metals

MDPI

Article

Study on Corrosion Behavior of Ultrafine-Grained Ti-6Al-7Nb Fabricated by Equal Channel Angular Pressing

Zequn Yu [1], Yuecheng Dong [1,2,*], Xin Li [1], Jingzhe Niu [3], Igor Alexandrov [4] and Hui Chang [1]

[1] College of Materials Science and Engineering/Tech Institute for Advanced Materials, Nanjing Tech University, Nanjing 211816, China; magicqqq3@163.com (Z.Y.); xinge@njtech.edu.cn (X.L.); ch2006@njtech.edu.cn (H.C.)
[2] State Key Laboratory of Metal Materials for Marine Equipment and Applications, Anshan 114000, China
[3] State Key Laboratory for Mechanical Behavior of Materials, Xi'an Jiaotong University, Xi'an 710049, China; njzhe91@gmail.com
[4] The Department of Physics, Ufa State Aviation Technical University, 450008 Ufa, Russia; igorvalexandrov@yandex.ru
* Correspondence: dongyuecheng@njtech.edu.cn; Tel.: +86-24-83587270

Received: 9 June 2020; Accepted: 13 July 2020; Published: 14 July 2020



Abstract: The aim of this study was to investigate the corrosion resistance of ultrafine-grained (UFG) Ti-6Al-7Nb fabricated by equal channel angular pressing (ECAP) and coarse-grained (CG) Ti- 6Al- 7Nb. The microstructure of each specimen was investigated by the electron backscattered diffraction (EBSD) method. The corrosion behavior of each specimen was determined by electrochemical measurement in Ringer's solution. The surface corroded morphologies and oxide film formed on Ti-6Al-7Nb alloy after electrochemical measurement were investigated by scanning electron microscope (SEM) and X-ray photoelectron spectroscopy (XPS). EBSD investigation shows that the grain size of UFG Ti-6Al-7Nb decreased to ~0.4 μm, accompanied by low angle grain boundaries (LAGBs) accounting for 39%. Potentiodynamic polarization and electrochemical impedance spectroscopy (EIS) results indicated that UFG Ti-6Al-7Nb alloy possessed a better corrosion resistance. The surface corroded morphologies revealed many small and shallow corrosion pits, which can be attributed to the good compactness of the oxide film and a rapid self- repairing ability of the UFG Ti-6Al-7Nb alloy.

Keywords: corrosion resistance; Ti-6Al-7Nb alloy; ultrafine-grained; equal channel angular pressing; oxide film

1. Introduction

Titanium and its alloys have been widely used in aerospace engineering, petro- and chemical engineering, as well as biomedical engineering due to their high specific strength, high corrosion resistance, low elastic modulus, and good biocompatibility [1–6]. Ti-6Al-4V alloy was first introduced as an engineering material becoming the most used titanium alloy worldwide. It has been widely applied in aircraft turbines [4,5], chemical equipment [7], and bio-implants [8] etc. Ti-6Al-7Nb alloy, a modified type of Ti-6Al-4V by replacing the toxic V by bio-inert Nb and maintaining the good mechanical properties, is considered as a better material for biomedical application [9,10]. Recently, ultrafine-grained (UFG) and nanocrystalline (NC) materials processed by severe plastic deformation (SPD) have been widely investigated and found to have unique physical and chemical properties [11–13]. Enhanced mechanical behavior and biocompatibility of UFG/NC Ti-6Al-7Nb alloy were acquired after the SPD process [14–19]. For instance, Polyakova et al. [9] revealed that the tensile strength of the UFG Ti-6Al-7Nb alloy with grain size of 330 nm increased to 1210 MPa after equal channel angular pressing (ECAP), which was 20% higher than observed in coarse-grained (CG) counterparts. Ashida et al. [15]

obtained a Ti-6Al-7Nb grain size of ~100 nm by high pressure and torsion (HPT) at room temperature. Results indicated that Vickers microhardness increases from 325 HV to 385 HV after HPT. Furthermore, the sample with refined grain size exhibited an excellent superplastic elongation of 930% at an initial strain rate of 2×10^{-3} s^{-1}. Oliveira et al. [16] reported that Ti-6Al-7Nb alloy processed by ECAP with an average grain size ~200 nm had higher fatigue properties, which make it suitable for practical application. At the same time, a highly bioactive behavior of UFG Ti- 6Al-7Nb alloy after phosphoric acid etching, regardless of the usage of alkaline treatment, was reported by Oliveira et al. [17].

Implanted biomedical materials have been immersed in human body fluids for several years, hence they are inevitably subject to attack by a corrosive environment. However, the corrosion behavior of UFG Ti-6Al-7Nb has not received enough attention and the effect of the refined grain size on corrosion resistance of titanium alloys is in dispute [20–27]. For instance, Legostaeva et al. [23] investigated the electrochemical behavior of CG and NC titanium and found that the dissolution rate of NC titanium increases in a Ringer–Locke solution in comparison with the CG state. However, Fattah-Alhosseini et al. [24] investigated the passivation and electrochemical response of NC titanium in Ringer's physiological solution and revealed that the passivation response of the NC sample improved compared to the CG state due to the formation of a thicker and less defective oxide film.

Therefore, the corrosion behavior of UFG Ti-6Al-7Nb alloy fabricated by ECAP was investigated by the methods of potentiodynamic polarization and electrochemical impedance spectroscopy (EIS) in Ringer's solution. The present study aimed to clarify the effect of the grain size on the corrosion resistance by considering the impact of other microstructural parameters and the formation of surface oxide film.

2. Materials and Methods

2.1. Materials

Grain refinement of Ti-6Al-7Nb alloy used in this study was conducted by the ECAP method (Ufa State Aviation Technical University, Ufa, Russia). Thermal treatment was used to obtain a CG sample after ECAP, which was annealed at 995 °C for 1 h, then annealed at 550 °C for 4 h followed by air cooling to form a "duplex" structure.

2.2. Microstructure Observation

Microstructure characterization of Ti-6Al-7Nb samples was performed by electron backscattered diffraction (EBSD) embedded in the Field Emission Scanning Electron Microscope (SEM, JSM-6700F, Jeol, Tokyo, Japan). Before the EBSD observation, the samples were mechanically polished to a mirror like surface by SiC paper followed by electro-polishing (solution: $HClO_4$:C_2H_5OH = 19:1 (volume ratio); voltage: 40 V; polishing time: 90 s). Automated EBSD scans were applied by Flamenco data acquisition software (Aztec 3.2, Oxford Instruments, Abingdon, United Kingdom). The average grain size and grain boundary orientation were processed with HKL Technology Channel 5 software (Oxford Instruments, Abingdon, United Kingdom).

2.3. Electrochemical Measurements

Corrosion behavior of Ti-6Al-7Nb samples was investigated by electrochemical testing in Ringer's solution (9 g/L NaCl, 0.42 g/L KCl, and 0.25 g/L $CaCl_2$) at pH 7.4. The experiment used a three-electrode system with the sample set as working electrode, the saturated Ag/AgCl electrode set as reference electrode, and a platinum piece set as auxiliary electrode. The surface of both tested samples and reference electrode were mechanically polished to a mirror like surface by SiC paper before each test. All tests were carried out by using electrochemical station (CHI660E, CH Instruments, Austin, TX, USA)) in a 37 °C water bath. The Open Circuit Potential was measured for 10 min. Electrochemical impedance spectroscopy (EIS) was performed at a frequency range from 100 kHz to 10 mHz with an AC voltage amplitude of ±10 mV. Potentiodynamic polarization data were acquired between –650 to

850 mV vs Ag/AgCl with 2 mV/s sweeping rate after the EIS test. Corroded morphology was observed by Scanning Electron Microscopy (SEM, JSM-6700F, Jeol, Tokyo, Japan) after the electrochemical tests.

2.4. Passivation Film Characterization

The samples' oxide film character was investigated by X-ray Photoelectron Spectroscopy (XPS), with an electron spectrometer (K-Alpha+, Thermo Scientific, Waltham, MA, USA). Al Ka was used as the X-ray source, the calibration of the photoelectron binding energy was performed using a C 1s signal with a binding energy of 284.8 eV. The surface chemical composition of the passivation film formed on the samples was fitted and analyzed by Avantage software (Avantage 5.9918, Thermo Scientific, Waltham, MA, USA).

3. Results

3.1. Microstructural Evolution

Figure 1 illustrated the microstructure and grain size distribution of different Ti-6Al-7Nb samples. It can be observed that fairly equiaxed and homogeneous grains exsist in the microstructure of the CG sample (Figure 1a), and the average grain size achieved 13.8 μm (Figure 1c). On the other hand, the microstructure of the UFG sample displays a remarkable grain refinement (Figure 1b), which can be attributed to the large volume of accumulative strain during the ECAP process. Although several non-uniform deformation areas were presented in the UFG Ti-6Al-7Nb sample, equiaxed and homogeneous microstructure were still revealed in the most part of the microstructure. The average grain size was reduced to 0.4 μm with volume fraction (~55%) located between 200–400 nm (Figure 1d).

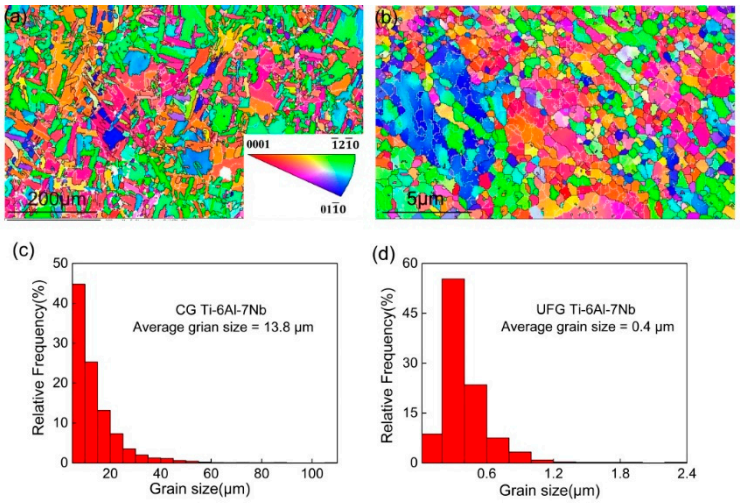


Figure 1. Electron backscattered diffraction (EBSD) results of microstructure (**a**,**b**) and grain size distribution (**c**,**d**) of coarse-grained (CG) (**a**,**c**) and ultrafine-grained (UFG) (**b**,**d**) Ti-6Al-7Nb.

Grain boundary and disorientated distribution of CG and UFG Ti-6Al-7Nb alloy are displayed in Figure 2. The black lines represent the high angle grain boundaries (HAGBs, $\theta > 15°$), while the red lines represent the low angle grain boundaries (LAGBs, $2° < \theta < 15°$). It can be seen that the grain boundary character changed obviously accompanied by an increase of grain size (Figure 2a,b) after heat treatment. The grain boundary character distribution indicates that the fraction of HAGBs could achieve 61% for the UFG state (Figure 2d) and increased to 77.6% (Figure 2c) for the CG counterparts. Furthermore, the fraction of HAGBs equal to 70° achieved 40% for the CG sample, which is different from the UFG state.

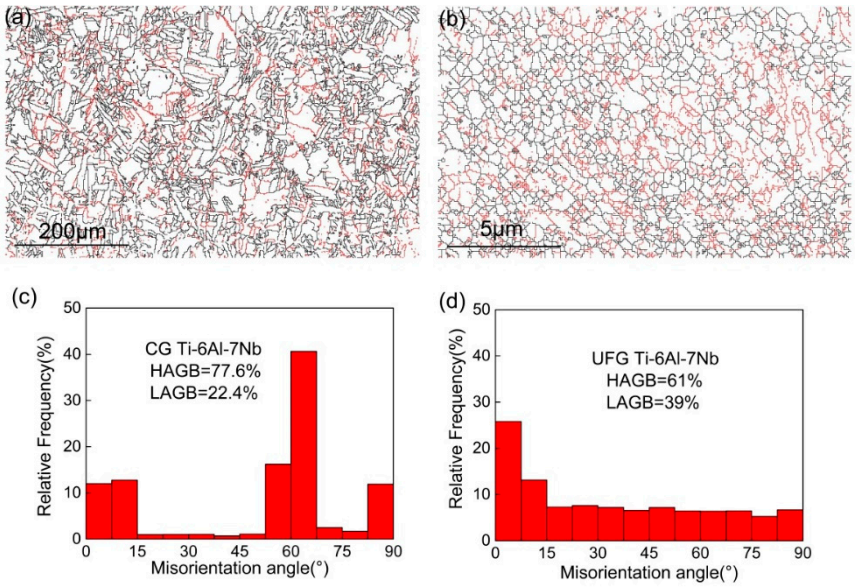


Figure 2. Grain boundary (**a**,**b**) and misorientation distribution (**c**,**d**) of coarse-grained (CG) (**a**,**c**) and ultrafine-grained (UFG) (**b**,**d**) Ti-6Al-7Nb alloy.

3.2. Corrosion Behavior

It can be seen from Figure 3 that the open circuit potential (OCP) value of the sample reached stability within 10 min. Figure 4 represents a typical potentiodynamic polarization curves of the samples in Ringer's solution. The Ti-6Al-7Nb alloys with different grain size exhibit a similar polarization behavior. It could be found that the pitting corrosion took place on both samples. As the potential increased to ~0.4 V vs Ag/AgCl, both the UFG and CG sample reached their stable passivation current densities. The anodic zone clearly revealed a similar current slope before passivation, which indicates the formation of passive film on the sample surface. After that, with the potential continually increasing, the current density changed significantly which indicated the occurrence of pitting corrosion. Table 1 illustrates the results of electrochemical parameters calculated from potentiodynamic polarization curves in Ringer's solution, the average value of these electrochemical parameters was obtained based on three valid data. E_{corr} is the corrosion potential while i_{corr} is the corrosion current density. Origin software was used to manually fit E_{corr} and i_{corr} by the Tafel extrapolation method. In general, corrosion rate R is proportional to i_{corr}, which can be calculated by Equation (1)

$$R = 3.27 \times 10^{-3} \frac{A \times i_{corr}}{n\rho} \quad (1)$$

where A represents the relative atomic mass, n and ρ represent the chemical valence state and density respectively.

Table 1. Results of electrochemical parameters calculated from potentiodynamic polarization curves.

Sample	E_{corr} ((V) vs. Ag/AgCl)	E_{pit} (V)	i_{pass} ($\mu A \cdot cm^{-2}$)	i_{corr} ($\mu A \cdot cm^{-2}$)	R ($mm \cdot a^{-1}$)
Coarse-Grained (CG)	−0.27 ± 0.01	0.33 ± 0.10	0.81 ± 0.25	0.33 ± 0.17	0.0028
Ultrafine-Grained (UFG)	−0.29 ± 0.05	0.45 ± 0.10	0.35 ± 0.10	0.14 ± 0.02	0.0012

Note: E_{corr}—corrosion potential, E_{pit}—pitting potential, i_{pass}—passivation current density, i_{corr}—corrosion current density, R—corrosion rate.

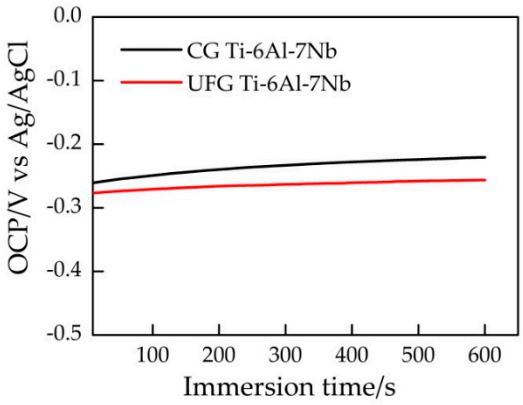


Figure 3. Electric potential-time curves of different samples in Ringer's solution.

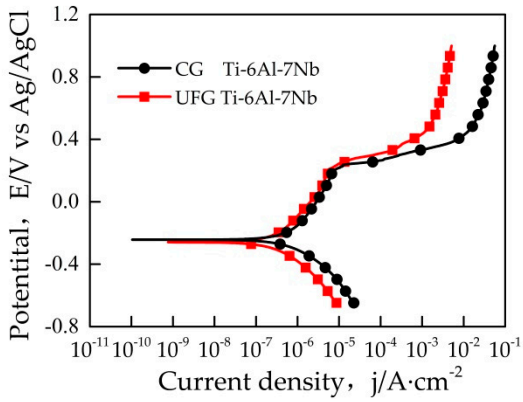


Figure 4. Potentiodynamic polarization curves of samples in Ringer's solution.

As can be seen from Table 1, the i_{pass} of the UFG Ti-6Al-7Nb is lower than the CG state, which implies that the passivation film of UFG Ti-6Al-7Nb possesses a better self-repairing ability. The E_{pit} of the UFG Ti-6Al-7Nb is higher than that of the CG state, which indicates that the pitting corrosion resistance of UFG sample has been improved. Generally, i_{corr} and R are used to characterize the corrosion resistance of materials intuitively [21], the values of i_{corr} and R of the UFG Ti-6Al-7Nb are much lower than the CG state, which indicates that the UFG Ti-6Al-7Nb sample possesses a better corrosion resistance.

Typical Nyquist diagrams for CG and UFG Ti-6Al-7Nb in Ringer's solution are presented in Figure 5. At the same time, Figure 5 shows an electrical equivalent circuit used to fit the experimental EIS data and evaluate the corrosion resistance of different Ti-6Al-7Nb samples. As can be seen in Figure 5, R_1 and CPE_1 represent the resistance and constant phase element of the passivation film, R_2 corresponds to the resistance of the charge-transfer reactions while CPE_2 represents the constant phase element of the electric double layer. The overall resistance of the material should be the sum of R_1 and R_2, which is the polarization resistance value (R_p). It is clearly shown in Figure 5 that the Nyquist diagram of the two tested samples demonstrates a similar semicircle, which implies that the same corrosion mechanism occurred. In general, the larger arc radius implies a better corrosion resistance of the sample [28–30]. The diameter of the semicircle for UFG Ti-6Al-7Nb is larger than the CG one, considering the exhibited higher polarization resistance (R_p) value of UFG Ti-6Al-7Nb alloy (Table 2), which means that the UFG Ti-6Al-7Nb alloy possesses a better corrosion resistance.

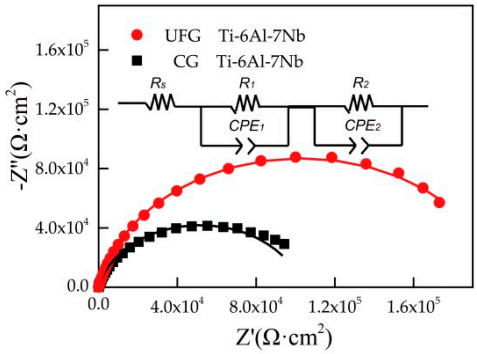


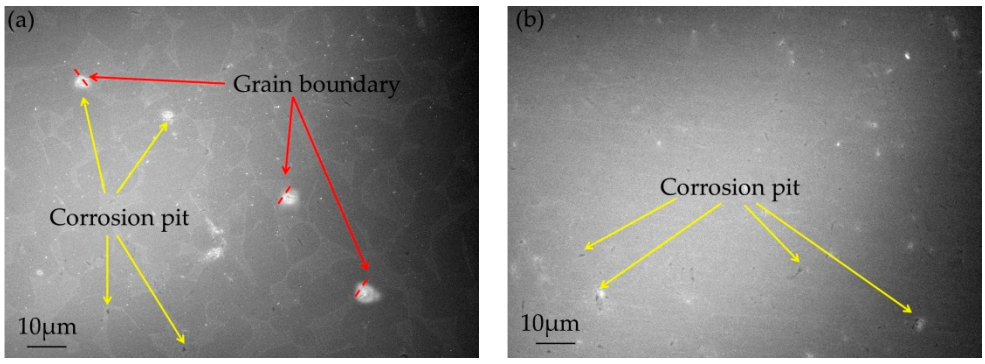
Figure 5. Typical Nyquist diagram for tested samples and the equivalent electric circuit for EIS data analysis (R_s—solution resistance, R_p—polarization resistance, R_1—resistance of passivation film, CPE_1—constant phase element of passivation film, R_2—resistance of charge-transfer reactions, CPE_2—constant phase element of the electric double layer, points represent experimental data while the solid lines represent electrical equivalent circuit fitting data).

Table 2. Results of electrochemical parameters calculated from electrochemical impedance spectroscopy (EIS) measurements.

Sample	R_s ($\Omega \cdot cm^2$)	CPE_1 (10^{-5} $S \cdot s^n \cdot cm^2$)	n_1	R_1 ($10^2 \Omega \cdot cm^2$)	CPE_2 (10^{-5} $S \cdot s^n \cdot cm^2$)	n_2	R_2 ($10^5 \Omega \cdot cm^2$)	R_p ($10^5 \Omega \cdot cm^2$)
CG	8.7 ± 1.7	8.5 ± 4.2	0.84 ±0.03	0.41 ± 0.12	4.7 ± 2.1	0.87 ± 0.01	1.1 ± 0.26	1.1 ± 0.26
UFG	12 ± 0.90	4.4 ± 2.9	0.90±0.05	30 ± 22	2.8 ± 0.31	0.94 ± 0.02	2.4 ± 0.16	2.4 ± 0.16

4. Discussion

Based on the experimental results above, it can be concluded that corrosion resistance of UFG Ti-6Al-7Nb is much better than that for CG. The surface corroded morphologies of CG and UFG Ti-6Al-7Nb after electrochemical experiments are shown in Figure 6. A few corrosion pits were generated on the surface of all test samples. In particular, the corrosion pits of CG Ti-6Al-7Nb are much bigger and deeper than the UFG ones, reaching as far as ~4 μm. For CG Ti-6Al-7Nb, some corrosion points show a brighter picture due to the oxide formation surrounding the point as oxides holds a higher electron capture ability under SEM. It seems that the corrosion pits occur at the grain boundaries and then extend, as indicated in Figure 6. The corrosion is more likely to occur and extend at the HAGBs due to high interfacial energy and impurity segregation [31,32], while the presence of LAGBs could block intergranular corrosion from the perspective of grain boundary engineering [33,34]. Meanwhile, it is worth pointing out that the grain boundary misorientation angle in UFG Ti- 6Al-7Nb distributes randomly, while the CG state concentrates at 70° (as shown in Figure 2), and corrosion pits can be found on the boundary.



(**a**) (**b**)

Figure 6. Corroded morphology of CG (**a**) and UFG (**b**) Ti-6Al-7Nb after electrochemical experiments.

Titanium and its alloys have good corrosion resistance, since an oxide film forms easily on the surface which can isolate the substrate of the metals from corrosive environments. Hence, the character of the oxide film plays an important role in the corrosion behavior of titanium alloys. As mentioned before, UFG Ti-6Al-7Nb alloy possesses a better ability on the oxide film of self-repairing, which can restrain the development of pitting when it occurs. It is well known that a large density of grain boundaries and dislocations can be generated with grain refinement in UFG Ti-6Al-7Nb during the SPD process. These defects could provide more nucleation sites for the oxide film and lead to a more rapid formation and a higher self-repairing ability of a passivation layer on the UFG Ti- 6Al- 7Nb alloy than for the CG [24,35].

XPS observations of the oxide film formed on CG and UFG Ti-6Al-7Nb are shown in Figure 7. As can be seen from the Ti 2p, Nb 3d and Al 2p XPS spectra, compositions of the oxide film for both tested samples are mainly composed of titanium, niobium, aluminum, and their oxides respectively (TiO_2, TiO, Ti_2O_3, Nb_2O_5, NbO, NbO_2, Al_2O_3). Among them, the Ti $2p_{3/2}$ peak and Ti $2p_{1/2}$ peak were located at 453.2 eV and 460 eV, the TiO_2 $2p_{3/2}$ peak and TiO_2 $2p_{1/2}$ peak were located at around 458.4 eV and 464 eV, the TiO $2p_{3/2}$ peak and TiO $2p_{1/2}$ peak were located at 454.8 eV and 460.2 eV, the Ti_2O_3 $2p_{3/2}$ peak and Ti_2O_3 $2p_{1/2}$ peak were located at 456.6 eV and 462.2 eV. The Nb $3d_{5/2}$ peak and Nb $3d_{3/2}$ peak were located at 202.4 eV and 205.1 eV, the Nb_2O_5 $3d_{5/2}$ peak and Nb_2O_5 $3d_{3/2}$ were located at 207 eV and 209.8eV, the NbO $3d_{5/2}$ peak and NbO $3d_{3/2}$ peak were located at 203.2 eV and 206.1 eV, the NbO_2 $3d_{5/2}$ peak and NbO_2 $3d_{3/2}$ peak were located at 204.2 eV and 207.1 eV. For the element Al, the center of the Al_2O_3 $2p_{3/2}$ peak was located at 74 eV, while the Al $2p_{3/2}$ peak was located at 71.5 eV.

The contents of titanium, niobium, aluminum, and their oxides were calculated and are listed in Table 3. As is well known, TiO_2 plays a more important role in corrosion resistance than other titanium oxides [36]. Obviously, the content of TiO_2 in the passivation film formed on UFG Ti- 6Al- 7Nb was higher than for CG. Also, the content of Nb2O5 in the UFG sample's passivation film was higher than for CG. The corrosion resistance and stability of Ti-6Al-7Nb alloy is much better than Ti-6Al-4V alloy, which is ascribed to the incorporation of niobium oxides, mainly Nb_2O_5 [37,38]. Furthermore, the existence of Nb^{5+} on the passivation film could lead to the excellent passivating properties of the anodically formed Ti(IV)-based surface oxide film and high corrosion resistance since Nb^{5+} can eliminate stoichiometric defects (anion vacancies) caused by the presence of titanium suboxides [39]. Besides that, titanium alloy with dense Ti and Nb oxide in the passivation film has better corrosion performance than Ti-6Al-4V, and its passivation range is larger [40]. It can be seen from Table 3 that the content of Al_2O_3 in the passivation film formed on UFG Ti-6Al-7Nb was lower than for CG. Al and its oxide Al_2O_3 in the passivation film could be attacked easily by the corrosive environment which may cause surface pitting corrosion. It is worth mentioning that the oxides in the passivation film have different solubilities in different simulated body fluid environments. Milošev [41] reported that Al_2O_3 has a higher solubility in artificial saliva containing fluoride ions in comparison to TiO_2 and Nb_2O_5, which indicate a worse corrosion resistance of Al_2O_3 than TiO_2 and Nb_2O_5. Finally, it can be concluded that good compactness of the passivation film could be formed on UFG Ti-6Al-7Nb which led to a better corrosion resistance.

Table 3. Content of titanium, niobium, aluminum, and corresponding oxides in the oxide film.

Composition (%)	TiO_2	Ti	Ti_2O_3	TiO	Nb_2O_5	Nb	NbO	NbO_2	Al_2O_3	Al
CG	79.61	1.23	14.10	5.06	87.23	7.62	4.57	0.58	92.78	7.22
UFG	86.91	0.84	7.94	4.31	91.57	4.21	3.43	0.79	82.70	17.30

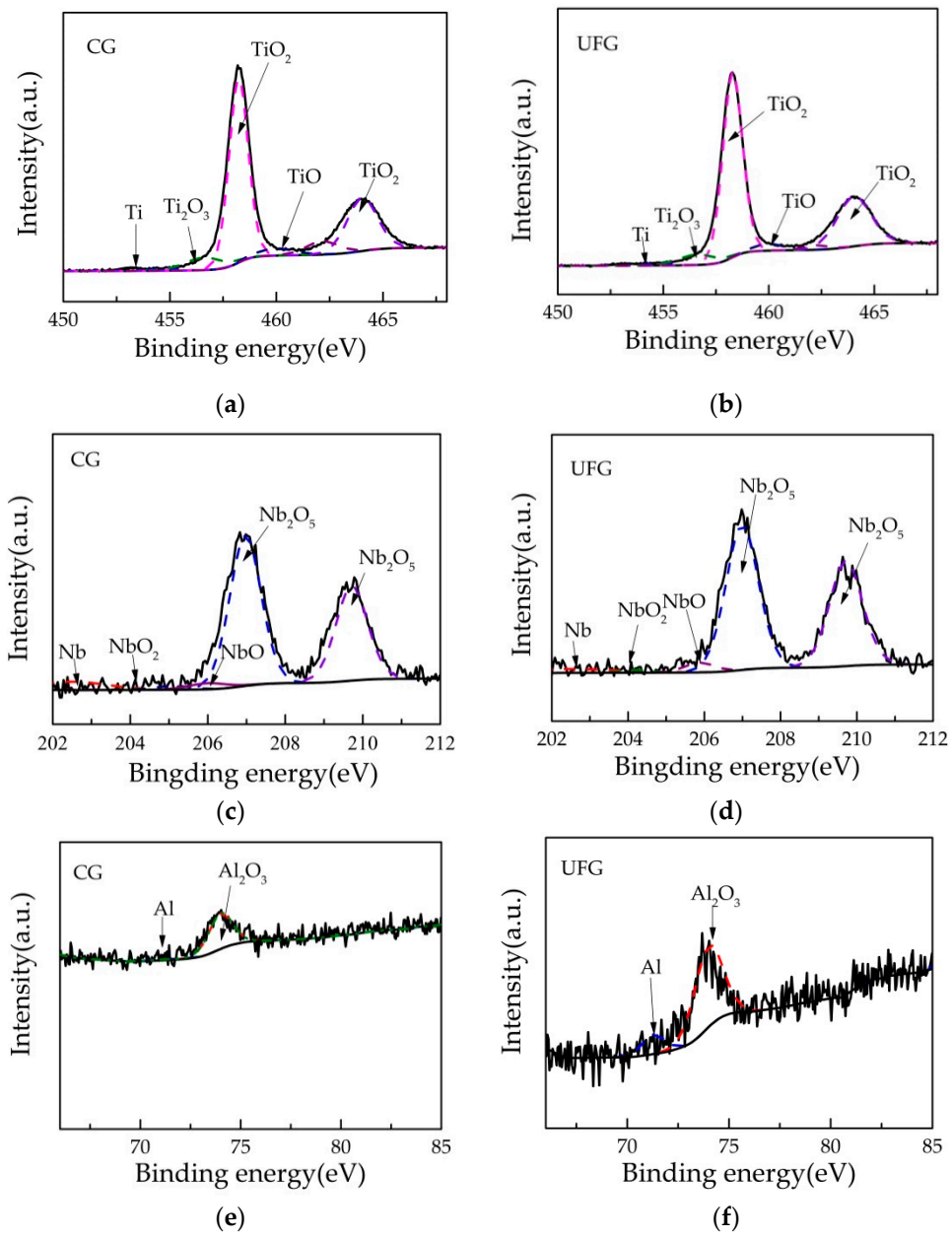


Figure 7. Detail Ti 2p, Nb 3d and Al 2p XPS spectra of the passivation film formed on (**a**,**c**,**e**) CG Ti-6Al-7Nb and (**b**,**d**,**f**) UFG Ti-6Al-7Nb on the surface.

5. Conclusions

The corrosion behavior of Ti-6Al-7Nb alloy fabricated by ECAP was investigated by the methods of potentiodynamic polarization and electrochemical impedance spectroscopy (EIS) in Ringer's solution in this study. The following conclusions can be drawn:

(1) The average grain size of UFG Ti-6Al-7Nb processed by ECAP reached 0.4 μm. After heat treatment at 995 °C/1 h + 550 °C/4 h, the grain size increased to 13.8 μm and the volume of LAGBs decreased from 39% to 22.4%;

(2) Electrochemical experiments indicated that UFG Ti-6Al-7Nb exhibits a lower corrosion current density and passivation current density than the CG state. The surface corroded morphologies of UFG Ti-6Al-7Nb revealed many small and shallow corrosion pits due to rapid self-repairing of the oxide film;

(3) Pitting corrosion can be found on all samples while the pitting points of the CG state sample are mainly located on the grain boundaries and further extended. The UFG sample shows a relative lower grain boundary corrosion due to a higher LAGB volume;

(4) Higher content of TiO_2 and Nb_2O_5 formed in the oxide film of UFG Ti-6Al-7Nb led to a denser passive film and thus ensured a better corrosion resistance.

Author Contributions: Conceptualization and methodology, Y.D., I.A. and H.C.; experimental investigation, calculation, writing—original draft preparation and editing, Z.Y.; data curation, Z.Y., X.L. and J.N.; writing—review and final version, project administration, funding acquisition, Y.D.; supervision, Y.D. and H.C. All authors have read and agreed to the published version of the manuscript.

Funding: This work was supported by State Key Laboratory Open Source for Metal Materials and Applications for Marine Equipment [SKLMEA-K201807], National Natural Science Foundation of China [51931008], the financial assistance from the China Postdoctoral Science Foundation [2017M623392], Priority Academic Program Development of Jiangsu higher education institutions [PAPD], Primary Research & Development Plan of Jiangsu Province [BE2019119].

Conflicts of Interest: The authors declare no conflict of interest.

References

1. Imai, K.; Zhou, X.; Liu, X.X. Application of Zr and Ti-Based Bulk Metallic Glasses for Orthopaedic and Dental Device Materials. *Metals* **2020**, *10*, 203. [CrossRef]
2. Amigo, A.; Vicente, A.; Afonso, C.R.M.; Amigo, V. Mechanical Properties and the Microstructure of beta Ti-35Nb-10Ta-*x*Fe Alloys Obtained by Powder Metallurgy for Biomedical Applications. *Metals* **2019**, *9*, 76. [CrossRef]
3. Kolli, R.P.; Devaraj, A. A Review of Metastable Beta Titanium Alloys. *Metals* **2018**, *8*, 506. [CrossRef]
4. González-Barrio, H.; Calleja-Ochoa, A.; Lamikiz, A.; Lacalle, L. Manufacturing Processes of Integral Blade Rotors for Turbomachinery, Processes and New Approaches. *Appl. Sci.* **2020**, *10*, 3063. [CrossRef]
5. Del Sol, I.; Rivero, A.; Lacalle, L.; Gámez, A. Thin-Wall Machining of Light Alloys: A Review of Models and Industrial Approaches. *Materials* **2019**, *12*, 2012. [CrossRef] [PubMed]
6. Ortiz, M.; Penalva, M.; Iriondo, E.; Lacalle, L. Investigation of Thermal-Related Effects in Hot SPIF of Ti–6Al–4V Alloy. *Int. J. Precis. Eng. Manuf.-Green Technol.* **2019**, *7*, 299–317. [CrossRef]
7. Gurrappa, I. Characterization of titanium alloy Ti-6Al-4V for chemical, marine and industrial applications. *Mater. Charact.* **2003**, *51*, 131–139. [CrossRef]
8. Patel, S.; Hamlekhan, A.; Royhman, D.; Butt, A.; Yuan, J.; Shokuhfar, T.; Sukotjo, C.; Mathew, M.; Jursich, G.; Takoudis, C. Enhancing surface characteristics of Ti–6Al–4V for bio-implants using integrated anodization and thermal oxidation. *J. Mater. Chem. B* **2014**, *2*, 3597–3608. [CrossRef]
9. Geetha, M.; Singh, A.K.; Asokamani, R.; Gogia, A.K. Ti based biomaterials, the ultimate choice for orthopaedic implants—A review. *Prog. Mater. Sci.* **2009**, *54*, 397–425. [CrossRef]
10. Tamilselvi, S.; Raman, V.; Rajendran, N. Corrosion behaviour of Ti–6Al–7Nb and Ti–6Al–4V ELI alloys in the simulated body fluid solution by electrochemical impedance spectroscopy. *Electrochim. Acta* **2007**, *52*, 839–846. [CrossRef]
11. Li, M.; Zhang, C.; Luo, J.; Fu, M. Thermomechanical coupling simulation and experimental study in the isothermal ECAP processing of Ti6Al4V alloy. *Rare Metals* **2010**, *29*, 613–620. [CrossRef]
12. Veverkova, A.; Kozlik, J.; Bartha, K.; Chraska, T.; Correa, C.A.; Strasky, J. Mechanical Properties of Ti-15Mo Alloy Prepared by Cryogenic Milling and Spark Plasma Sintering. *Metals* **2019**, *9*, 1280. [CrossRef]
13. Valiev, R.; Semenova, I.P.; Jakushina, E.; Latysh, V.V.; Rack, H.J.; Lowe, T.C.; Petruželka, J.; Dluhoš, L.; Hrušák, D.; Sochová, J. Nanostructured SPD Processed Titanium for Medical Implants. *Mater. Sci. Forum* **2008**, *584–586*, 49–54. [CrossRef]
14. Polyakova, V.V.; Semenova, I.P.; Polyakov, A.V.; Magomedova, D.K.; Huang, Y.; Langdon, T.G. Influence of grain boundary misorientations on the mechanical behavior of a near-α Ti-6Al-7Nb alloy processed by ECAP. *Mater. Lett.* **2017**, *190*, 256–259. [CrossRef]
15. Ashida, M.; Chen, P.; Doi, H.; Tsutsumi, Y.; Hanawa, T.; Horita, Z. Superplasticity in the Ti–6Al–7Nb alloy processed by high-pressure torsion. *Mater. Sci. Eng. A* **2015**, *640*, 449–453. [CrossRef]

16. Oliveira, D.P.; Prokofiev, E.; Sanches, L.F.R.; Polyakova, V.; Valiev, R.Z.; Botta, W.J.; Junior, A.M.J.; Bolfarini, C. Surface chemical treatment of ultrafine-grained Ti–6Al–7Nb alloy processed by severe plastic deformation. *J. Alloy. Compd.* **2015**, *643*, S241–S245. [CrossRef]
17. Oliveira, D.P.; Toniato, T.V.; Ricci, R.; Marciano, F.R.; Prokofiev, E.; Valiev, R.Z.; Lobo, A.O.; Jorge Júnior, A.M. Biological response of chemically treated surface of the ultrafine-grained Ti-6Al-7Nb alloy for biomedical applications. *Int. J. Nanomed.* **2019**, *14*, 1725–1736. [CrossRef]
18. Gabitova, S.; Polyakova, V.; Semenova, I. Enhanced fatigue strength of ultrafine-grained Ti-6Al-7Nb ELI alloy: Microstructural aspects and failure peculiarities. *Rev. Adv. Mater. Sci.* **2012**, *31*, 123–128.
19. Gallego, J.; Pinheiro, T.; Valiev, R.; Polyakova, V.; Bolfarini, C.; Kiminami, C.; Jorge Junior, A.; Botta, W. Microstructural Characterization of Ti-6Al-7Nb Alloy After Severe Plastic Deformation. *Mater. Res.* **2012**, *15*, 786–791. [CrossRef]
20. Balyanov, A.; Kutnyakova, J.; Amirkhanova, N.A.; Stolyarov, V.V.; Valiev, R.Z.; Liao, X.Z.; Zhao, Y.H.; Jiang, Y.B.; Xu, H.F.; Lowe, T.C. Corrosion resistance of ultra fine-grained Ti. *Scr. Mater.* **2004**, *51*, 225–229. [CrossRef]
21. Nie, M.; Wang, C.T.; Qu, M.; Gao, N.; Wharton, J.A.; Langdon, T.G. The corrosion behaviour of commercial purity titanium processed by high-pressure torsion. *J. Mater. Sci.* **2014**, *49*, 2824–2831. [CrossRef]
22. Garbacz, H.; Pisarek, M.; Kurzydłowski, K.J. Corrosion resistance of nanostructured titanium. *Biomol. Eng.* **2007**, *24*, 559–563. [CrossRef]
23. Legostaeva, E.V.; Egorkin, V.S.; Sinebryukhov, S.L.; Eroshenko, A.Y.; Lyamina, G.V.; Komarova, E.G.; Gnedenkov, S.V.; Sharkeev, Y.P. Nanostructured titanium: Structure, mechanical and electrochemical properties. *Inorg. Mater. Appl. Res.* **2014**, *5*, 44–53. [CrossRef]
24. Fattah-Alhosseini, A.; Imantalab, O.; Ansari, G. The role of grain refinement and film formation potential on the electrochemical behavior of commercial pure titanium in Hank's physiological solution. *Mater. Sci. Eng. C* **2017**, *71*, 827–834. [CrossRef] [PubMed]
25. Krüger, L.; Schwarz, F.; Mandel, M.; Hockauf, M. Electrochemical corrosion studies of ultrafine-grained aluminium alloy EN AW-6063. *Mater. Corros.* **2015**, *66*, 226–232. [CrossRef]
26. Jiang, J.H.; Ma, A.B.; Lu, F.M.; Saito, N.; Watazu, A.; Song, D.; Zhang, P.; Nishida, Y. Improving corrosion resistance of Al-11mass%Si alloy through a large number of ECAP passes. *Mater. Corros.* **2011**, *62*, 848–852. [CrossRef]
27. Li, S.; Beyerlein, I.J.; Alexander, D.J.; Vogel, S.C. Texture evolution during multi-pass equal channel angular extrusion of copper: Neutron diffraction characterization and polycrystal modeling. *Acta Mater.* **2005**, *53*, 2111–2125. [CrossRef]
28. Yang, D.S.; Dong, Y.C.; Chang, H.; Alexandrov, I.; Li, F.; Wang, J.T.; Dan, Z.H. Corrosion behavior of ultrafine-grained copper processed by equal channel angular pressing in simulated sea water. *Mater. Corros.* **2018**, *69*, 10. [CrossRef]
29. Çomaklı, O.; Yazıcı, M.; Yetim, T.; Yetim, A.; Celik, A. The effect of calcination temperatures on structural and electrochemical properties of TiO_2 film deposited on commercial pure titanium. *Surf. Coat. Technol.* **2016**, *285*, 298–303. [CrossRef]
30. Jin, L.; Cui, W.-F.; Song, X.; Liu, G.; Zhou, L. Effects of surface nanocrystallization on corrosion resistance of β-type titanium alloy. *Trans. Nonferrous Metals Soc. China* **2014**, *24*, 2529–2535. [CrossRef]
31. Zhao, Y.; Cheng, I.C.; Kassner, M.E.; Hodge, A.M. The effect of nanotwins on the corrosion behavior of copper. *Acta Mater.* **2014**, *67*, 181–188. [CrossRef]
32. Kim, S.H.; Erb, U.; Aust, K.T.; Palumbo, G. Grain boundary character distribution and intergranular corrosion behavior in high purity aluminum. *Scr. Mater.* **2001**, *44*, 835–839. [CrossRef]
33. Hu, C.; Xia, S.; Li, H.; Liu, T.; Zhou, B.; Chen, W.; Wang, N. Improving the intergranular corrosion resistance of 304 stainless steel by grain boundary network control. *Corros. Sci.* **2011**, *53*, 1880–1886. [CrossRef]
34. Michiuchi, M.; Kokawa, H.; Wang, Z.J.; Sato, Y.S.; Sakai, K. Twin-Induced grain boundary engineering for 316 austenitic stainless steel. *Acta Mater.* **2006**, *54*, 5179–5184. [CrossRef]
35. Jelliti, S.; Richard, C.; Retraint, D.; Roland, T.; Chemkhi, M.; Demangel, C. Effect of surface nanocrystallization on the corrosion behavior of Ti–6Al–4V titanium alloy. *Surf. Coat. Technol.* **2013**, *224*, 82–87. [CrossRef]
36. Xiaojia, Y.; Du, C.; Wan, H.; Liu, Z.-Y.; Li, X. Influence of sulfides on the passivation behavior of titanium alloy TA2 in simulated seawater environments. *Appl. Surf. Sci.* **2018**, *458*, 198–209.

37. Milošev, I.; Kosec, T.; Strehblow, H.H. XPS and EIS study of the passive film formed on orthopaedic Ti–6Al–7Nb alloy in Hank's physiological solution. *Electrochim. Acta* **2008**, *53*, 3547–3558. [CrossRef]
38. Milošev, I.; Metikoš-Huković, M.; Strehblow, H.H. Passive film on orthopaedic TiAlV alloy formed in physiological solution investigated by X-ray photoelectron spectroscopy. *Biomaterials* **2000**, *21*, 2103–2113. [CrossRef]
39. Metikos-Huković, M.; Kwokal, A.; Piljac, J. The influence of niobium and vanadium on passivity of titanium-based implants in physiological solution. *Biomaterials* **2003**, *24*, 3765–3775. [CrossRef]
40. Bai, Y.; Li, S.J.; Prima, F.; Hao, Y.L.; Yang, R. Electrochemical corrosion behavior of Ti–24Nb–4Zr–8Sn alloy in a simulated physiological environment. *Appl. Surf. Sci.* **2012**, *258*, 4035–4040. [CrossRef]
41. Milošev, I.; Kapun, B.; Šelih, V. The Effect of Fluoride Ions on the Corrosion Behaviour of Ti Metal, and Ti6-Al-7Nb and Ti-6Al-4V Alloys in Artificial Saliva. *Acta Chim. Slov.* **2013**, *60*, 543–555. [PubMed]



© 2020 by the authors. Licensee MDPI, Basel, Switzerland. This article is an open access article distributed under the terms and conditions of the Creative Commons Attribution (CC BY) license (http://creativecommons.org/licenses/by/4.0/).